Analysis and Control of Flow-Acoustic Feedback-Loop Interactions in Transitional Airfoils

Vladimir GOLUBEV[1]; Lap NGUYEN[2], Reda MANKBADI[3]; Michel ROGER[4]

[1, 2, 3] FCAAP, Embry-Riddle Aeronautical University, USA

[4] LMFA, Ecole Centrale de Lyon, France

ABSTRACT

Our recent numerical and experimental efforts are reviewed examining flow-acoustic resonant interactions in transitional airfoil boundary layers and means of control of the resulting prominent, tonal trailing-edge noise sources. Experimentally recorded unsteady responses of loaded, transitional NACA0012 airfoil reveal operational regimes characterized by the presence of the shifted ladder-type tonal structures with dual velocity dependence observed in the surface pressure and the acoustic signals. High-fidelity numerical efforts employ a 6th-order Navier-Stokes solver implementing a low-pass filtering of poorly resolved high-frequency solution content to retain numerical accuracy and stability over a range of transitional flow regimes. 2D and 3D (ILES) numerical experiments investigate the behavior of the boundary-layer statistical moments during the transitional flow regimes characterized by the presence of separation regions and the resulting formation of the highly-amplified instability waves scattered into noise at the airfoil trailing edge, thus triggering and sustaining the acoustic feedback-loop process. The current paper particularly focuses on the sensitivity of the airfoil flow-acoustic interactions (and the resulting acoustic signature) to the upstream flow conditions.

Keywords: Flow-Acoustic Interactions, Transitional Airfoil, ILES
I-INCE Classification of Subjects Number: 13.1.1

1. INTRODUCTION

The subject of flow-acoustic resonant interactions generally encompasses a number of interfering physical phenomena. Their intricate interplay renders this area of research a particularly challenging task, with inherently multi-scale physics sometimes poorly understood. The flow-acoustic interactions are usually characterized by the presence of self-sustained shear-layer flow instabilities coupled with a resonant acoustic feedback mechanism. For high-speed flows, the examples of jet screech and cavity oscillations are well known and have been extensively studied in numerous works reviewed, e.g., by Raman (1) and Colonius (2) both from the basic physics and the flow control prospective.

The current work, on the other hand, addresses related phenomena for wall-bounded (rather than free-shear) airfoil flows and at low speeds, which have been treated less extensively in the past and still remain the subject of some controversy, as reviewed in reference (3). It is recognized that distinct acoustic signatures generated by small aircraft, low-speed rotors and fans, and wind-turbine blades are inherently linked to the isolated airfoil trailing-edge tones which are suddenly (and, in fact, often intermittently) produced during certain transitional flow regimes. The first comprehensive experimental study by Paterson et al (4) focused on tonal noise emitted by symmetric NACA airfoils in a Reynolds number range corresponding to full-scale helicopter rotors. Their key finding illustrated in Fig. 1 shows an unusual ladder-type structure (staging) of tones wherein the peak frequencies are scaled ~$U^{1.5}$ (U is the free-stream velocity) with sudden jumps appearing between the rungs of the ladder scaled ~$U^{0.8}$. Tam (5) proposed a feedback-loop mechanism to explain the tonal staging, with his original scenario of localized wake source corrected and further elaborated by Arbey & Bataille (6) based on a series of experiments with NACA0012 airfoils. Their recorded acoustic spectra generally

[1] golubd1b@erau.edu
[2] nguye276@erau.edu
[3] mankbadr@erau.edu
[4] Michel.Roger@ec-lyon.fr

confirmed the tonal ladder structure of Paterson et al (1973) to produce, for a given velocity in the range of U=20…40 m/s (Re_c=2…6×10^5), a narrowband set of equidistant frequencies superimposed on a broadband hump. In the interpretation first suggested by Longhouse (7), such contribution was attributed to Tollmien-Schlichting (T-S) instability waves developing in the boundary layer and scattering as sound at the airfoil trailing edge. The acoustic feedback loop was presumed to be generated between selected trailing-edge frequency tones and the most amplified T-S wave based on the condition that both sound and convected waves are in phase at the point of the instability appearance.

In reference (2), we re-visited the problem using complementary experimental and numerical studies investigating the presence of the flow-acoustic feedback interactions in NACA0012 airfoil in the transitional flow regimes. In particular, parametric experimental studies were conducted both with uniform and low-turbulence inflows, with boundary-layer tripping (on one or both sides) and without tripping, at different angles of attack, and for a range of flow speeds corresponding to M=0.03...0.15 (Re_c= 0.5×10^5...3×10^5). Some results of these studies are reviewed in the current work. The numerical approach employed high-accuracy 2D analysis based on the assumption that the investigated flow regimes retain primarily laminar boundary-layer structures. In other words, although the local separation zones should induce inherently 3D structures, the breakdown process was presumed to be at an early transitional stage so that the mechanism of the tonal noise generation could still be well described using 2D analysis. More recently, a comprehensive 3D Implicit Large-Eddy Simulation (ILES) study has been conducted to test such assumption, with the comparison against the 2D study discussed below. Particular emphasis is on the ability of both analyses to accurately resolve the laminar separation zones shown to play a major role in the instability amplification, saturation and preservation dominating the feedback-loop interaction process.

The current numerical efforts include a study of the effect of upstream turbulence with different intensity levels on the flow-acoustic resonant interactions and the resulting unsteady aerodynamic and acoustic airfoil responses. The results are further compared with linear stability analyses to examine the amplification rates and the accumulated growth of the dominant frequency modes for different upstream flow conditions.

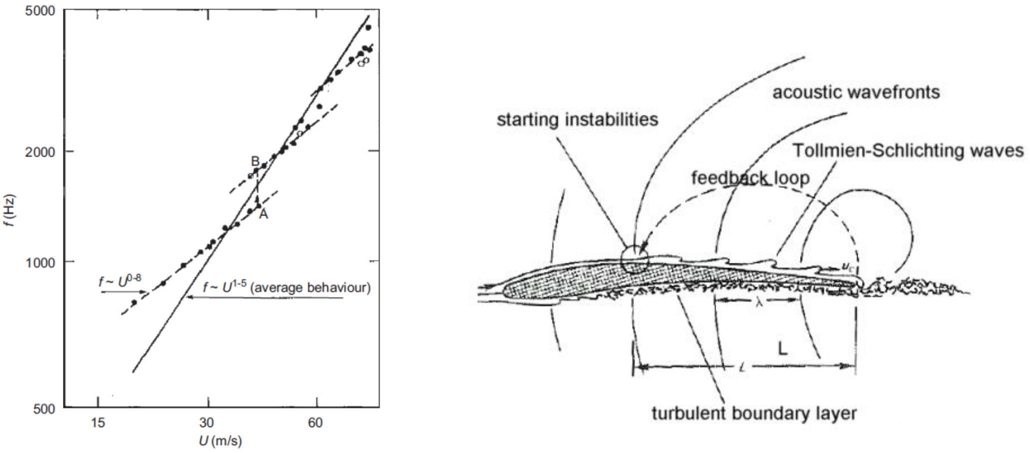

Figure 1 – Left: airfoil ladder-type frequency structure, from Paterson et al (4). Right: feedback loop in airfoil flow-acoustic interactions, from Longhouse (7).

2. EXPERIMENTAL RESULTS

Experiments (2) conducted in anechoic low-speed wind tunnel facility at Ecole Centrale de Lyon (ECL) (Fig. 2) examined the tonal signature of the low-speed NACA0012 airfoils for a range of transitional flow regimes characterized by variable flow velocity, angle of attack, and unsteady inflow conditions to carefully map regions of tonal production including effects of upstream unsteadiness. Far-field acoustic measurements were performed in the mid-span plane using a single microphone on a rotating arm to provide an overview of frequency-angle characterization and spectral directivity of the sound. The wall-pressure fluctuations were measured using remote-microphone probes (RMPs) flush-mounted along the airfoil surface at the locations shown in Fig. 3.

Figure 2 - Picture of ECL facility showing the nozzle flow and the horizontal end-plates.

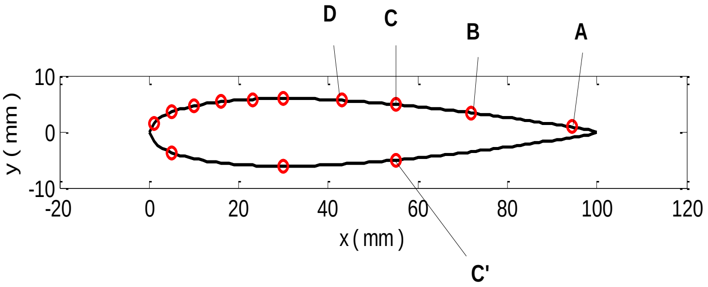

Figure 3 - Locations of RMPs on NACA-0012 mock-up (red symbols) and reference points for the analysis of wall-pressure fluctuations.

Additional measurements included hot-wire traversing probe analysis of the near-wake velocity profiles (2 mm downstream of the trailing edge) and flow visualizations that employed distemper fluid to examine laminar, turbulent and/or separated boundary layer regions and particularly identify the presence of laminar separation bubbles in the test case studies.

Tests were conducted with rectangular airfoil sections of 8cm and 10cm chords and of 30 cm span (aspect ratio of nearly 3), both in clean flow and with controlled inflow disturbance, with boundary-layer tripping (on one or both sides) and without tripping, at different angles of attack, and for a range of flow speeds corresponding to M=0.03...0.15 (Re_c= $0.5\times10^5...3\times10^5$). Tripping a transitional boundary layer forces transition to turbulence thus eliminating the onset of coherent instabilities. The one-side tripping was suggested by results from the DNS study of Desquesnes et al (8) who proposed another view on the multi-tone acoustic response involving interaction of the main and the secondary feedback loops on both sides of the airfoil. However, the present results demonstrate that the ladder-type acoustic tonal structure may reveal itself without such interaction. This is emphasized in Fig. 4 where the noise amplitude measured at 90° to the flow and at 2 m in the mid-span plane is plotted as a function of frequency and flow speed. The results were obtained for the one-side tripped airfoil of 8 cm chord, at geometrical angles of attack -5°, 0° and +5°. Apart from the low-frequency contribution at the bottom right corner of each color map, the tonal signature is clearly observed in each case, with different amplitudes and frequency ranges. The global oblique trace follows f_s~$U^{1.5}$ (yellow patterns) though the trend is less pronounced for Configuration B. Superimposed in red are the lines (rungs) corresponding to tones with f~$U^{0.8...0.85}$. Overall, multiple tones are observed at a given flow speed, as shown in Fig. 4 and further in Fig. 5.

The clearest ladder-type structure is found at zero angle of attack (Configuration A) and is close to observations by Arbey & Bataille (6). In Configuration B, the tripping is on the airfoil pressure side and the sound originates from instabilities amplifying along the suction side. The tones are less numerous and at much lower level but, in contrast, they can be detected at lower flow speeds. In Configuration C, the tripping is on the suction side and visualizations suggest that flow separates over a large part of the pressure-side boundary layer. Multiple tones are also detected but with a less organized structure. Moreover, their occurrence requires significantly higher flow speed.

Based on the obtained experimental data, it may be concluded that two separate phenomena are, in fact, at play in the observed ladder-type structures of acoustic tones. The rungs with f~$U^{0.8}$ are related to the amplified instability waves' trailing-edge scattering, while the effectively produced vortex shedding corresponds to the dominant frequencies of each rung scaled with f_s~$U^{1.5}$.

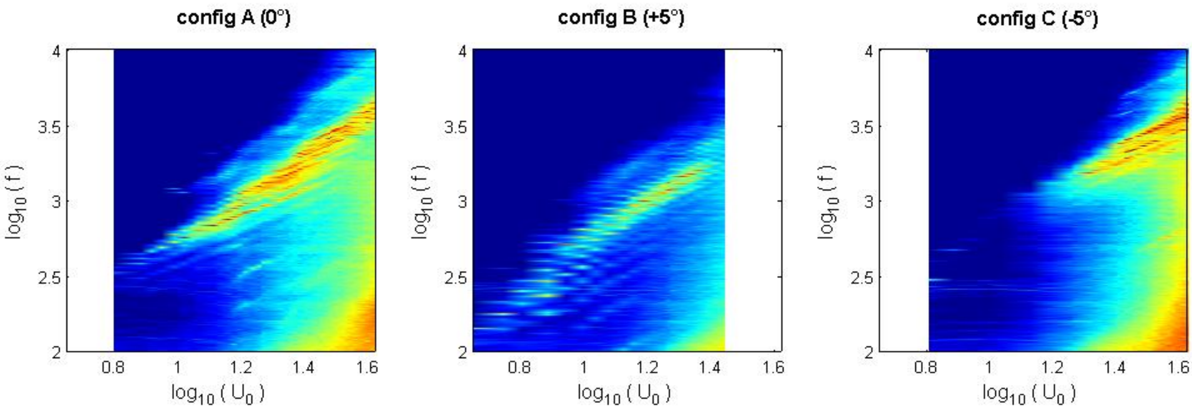

Figure 4 - Frequency versus flow-speed charts of airfoil tonal noise. One-side tripped NACA0012, 8 cm chord length, tripping strip on the pressure side (+5°) and on the suction side (-5°).

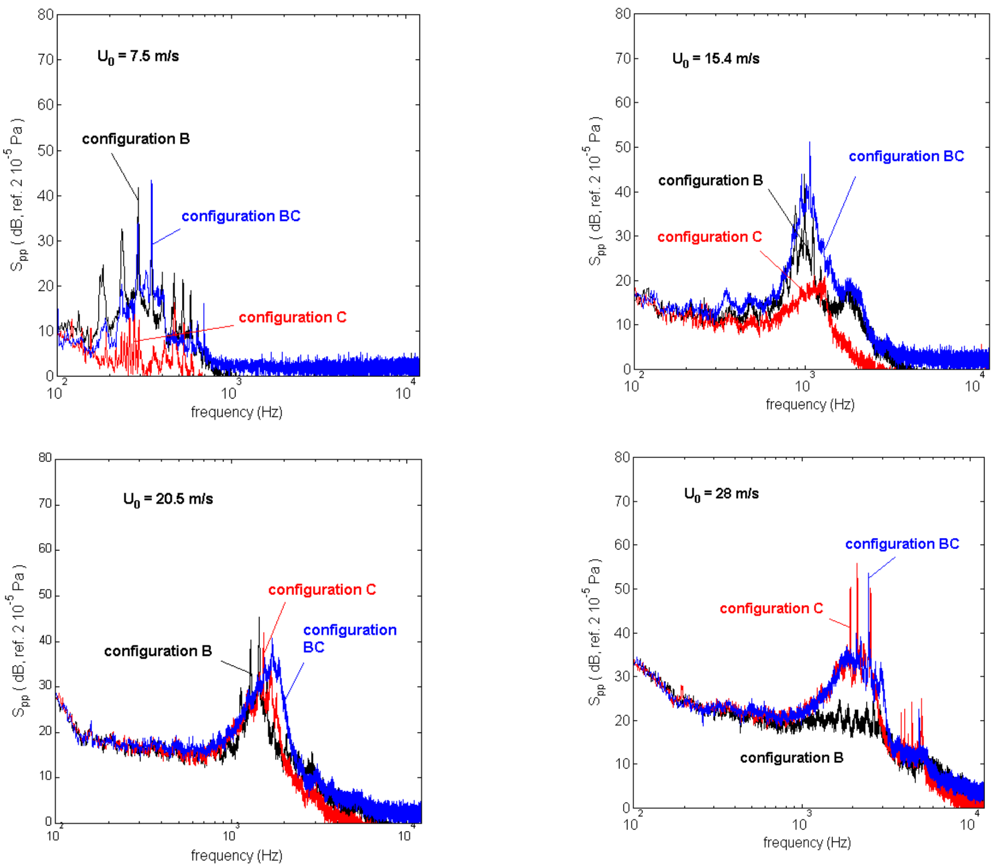

Figure 5 - Typical sound spectra measured at 5° angle of attack, at various flow speeds. B: tripping on pressure side, C: tripping on suction side, BC: no tripping.

To show the effect of a non-uniform inflow on flow-acoustic resonant interactions, experiments were also conducted with a *weak* grid-generated upstream turbulence. The grid mesh installed in the nozzle duct was of 1 cm width, and the diameter of the mesh wires was 1.5 mm. The turbulence spectrum measured in the presence of the grid fitted well with the homogeneous isotropic von Kármán model accounting for an additional Gaussian attenuation to reproduce the drop towards the Kolmogorov scale (with cut-off frequency around 9500 Hz). The corresponding integral length scale was 3.5 mm and the rms velocity was 0.2 m/s (0.8 % turbulence rate). The results in Fig. 6 (compare with Fig. 4) show that the external boundary-layer excitation suppresses all tones associated with the acoustic feedback (i.e., 0.8-power dependence in the ladder-type tonal structure) while the 1.5-power dependence is still preserved for the low turbulence intensity. Further details of this experimental study may be found in reference (2) but the effects of the upstream turbulence are further discussed below based on the results of numerical simulations.

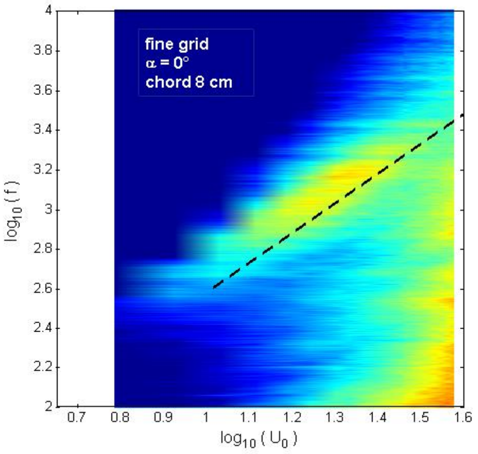

Figure 6 - Frequency versus flow-speed charts for a symmetrical NACA-0012 airfoil of 8 cm chord length set at 0° (left) and 5° (right) angles of attack in low-intensity upstream turbulence.

3. NUMERICAL FORMULATION

The employed numerical formulation (9) solves a set of the compressible Navier-Stokes equations represented in strong, conservative, time-dependent form in the generalized curvilinear computational coordinates (ξ,η,ζ,τ) transformed from the physical coordinates (x,y,z,t):

$$\frac{\partial}{\partial\tau}\left(\frac{\vec{Q}}{J}\right)+\frac{\partial\vec{F}_i}{\partial\xi}+\frac{\partial\vec{G}_i}{\partial\eta}+\frac{\partial\vec{H}_i}{\partial\zeta}+\frac{1}{\mathrm{Re}}\left[\frac{\partial\vec{F}_v}{\partial\xi}+\frac{\partial\vec{G}_v}{\partial\eta}+\frac{\partial\vec{H}_v}{\partial\zeta}\right]=\vec{S} \tag{1}$$

The solution vector $\vec{Q}=(\rho,\rho u,\rho v,\rho w,\rho e)$ is defined in terms of the flow density ρ, Cartesian flow velocity components (u, v, w), and flow specific energy,

$$e=\frac{T}{\gamma(\gamma-1)M_\infty^2}+\frac{1}{2}(u^2+v^2+w^2) \tag{2}$$

with assumed perfect gas relationship $p=\rho T/\gamma M_\infty^2$ connecting the flow pressure p, temperature T, and the freestream Mach number M_∞ (γ is the specific heat ratio). The other variables in Eq. (1) include the inviscid flux vectors defined by,

$$\vec{F}_i=\begin{bmatrix}\rho\hat{u}\\ \rho u\hat{u}+\hat{\xi}_x p\\ \rho v\hat{u}+\hat{\xi}_y p\\ \rho w\hat{u}+\hat{\xi}_z p\\ (\rho e+p)\hat{u}-\hat{\xi}_t p\end{bmatrix},\quad \vec{G}_i=\begin{bmatrix}\rho\hat{v}\\ \rho u\hat{v}+\hat{\eta}_x p\\ \rho v\hat{v}+\hat{\eta}_y p\\ \rho w\hat{v}+\hat{\eta}_z p\\ (\rho e+p)\hat{v}-\hat{\eta}_t p\end{bmatrix},\quad \vec{H}_i=\begin{bmatrix}\rho\hat{w}\\ \rho u\hat{w}+\hat{\zeta}_x p\\ \rho v\hat{w}+\hat{\zeta}_y p\\ \rho w\hat{w}+\hat{\zeta}_z p\\ (\rho e+p)\hat{w}-\hat{\zeta}_t p\end{bmatrix}, \tag{3}$$

the transformation Jacobian, $J=\partial(\xi,\eta,\zeta,\tau)/\partial(x,y,z,t)$, the metric quantities defined, e.g., as $\hat{\xi}_x=(J^{-1})\partial\xi/\partial x$, etc., and the transformed flow velocity components,

$$\begin{aligned}\hat{u} &= \hat{\xi}_t + \hat{\xi}_x u + \hat{\xi}_y v + \hat{\xi}_z w \\ \hat{v} &= \hat{\eta}_t + \hat{\eta}_x u + \hat{\eta}_y v + \hat{\eta}_z w \\ \hat{w} &= \hat{\zeta}_t + \hat{\zeta}_x u + \hat{\zeta}_y v + \hat{\zeta}_z w\end{aligned} \quad (4)$$

The viscous flux vectors in equation (1) are defined, e.g., in reference (10), while S represents the source term which in the current work generates an incompressible upstream turbulence upstream of the wing section. All flow variables are normalized by their respective reference freestream values except for pressure which is nondimensionalized by $\rho_\infty u_\infty^2$.

Note that the governing equations are represented in the original unfiltered form used unchanged in laminar, transitional or fully turbulent regions of the flow, with reference (11) providing further details on the code's employed ILES procedure in which a high-order low-pass filter operator is applied to the dependent variables during the solution process, in contrast to the standard LES addition of sub-grid stress (SGS) and heat flux terms. The resulting filter selectively damps the evolving poorly resolved high-frequency content of the solution.

The code employs a finite-difference approach to discretize the governing equations, with all the spatial derivatives obtained using the high-order compact-differencing schemes from reference (12). For the wing section computations of the current paper, a sixth-order scheme is used. At boundary points, higher-order one-sided formulas are utilized which retain the tridiagonal form of the scheme. In order to ensure that the Geometric Conservation Law (GCL) is satisfied, the time metric terms are evaluated employing the procedures described in detail in reference (11). Finally, the time marching is accomplished by incorporating a second-order iterative, implicit approximately-factored procedure as described, e.g., in reference (9).

4. NUMERICAL RESULTS

The original 2D numerical study of reference (2) employed a 643 × 395 × 3 O-mesh generated about NACA0012 airfoil and efficiently partitioned into sets of overlapped blocks assigned to different processors during parallel implementations. The mesh was carefully clustered near the airfoil surface to achieve the wall-normal and wall-tangent mesh sizes of $\Delta y/c=5\times10^{-5}$ and $\Delta x/c=10^{-3}$. In terms of the wall units $y_w^+/c=6.2\times10^{-5}$ estimated for the characteristic flow condition with M=0.1 and $Re_c=2\times10^5$, such grid refinement corresponds to the non-dimensional values of $\Delta y^+\approx1$ and $\Delta x^+=20$, with 12 grid points clustered in the region $0< y^+<10$. For 3D simulations, such grid parameters correspond to a high-resolution LES according to estimates in Wagner et al (13) (p.209). The grid is also finer compared to the mesh employed in a similar DNS study by Desquesnes et al (8) conducted using the mesh with $\Delta y/c=3.8\times10^{-4}$ and $\Delta x/c=6\times10^{-3}$.

Table 1 - Grids employed in 2D and 3D studies.

Cases	Dimension	Δy/c	Δx/c
2D BASE	**643 × 395 × 3**	**5.0×10^{-5}**	**1.0×10^{-3}**
2D FINE	**1281 × 789 × 3**	**2.5×10^{-5}**	**0.5×10^{-3}**
2D FINEST	**2569 × 789 × 3**	**2.5×10^{-5}**	**0.25×10^{-3}**
3D BASE	**643 × 395 × 81**	**5.0×10^{-5}**	**1.0×10^{-3}**
3D FINE	**964 × 592 × 81**	**3.75×10^{-5}**	**0.75×10^{-3}**

The 2D approach may be justified based on the assumption that though inherently unsteady, the investigated flow regimes remain primarily laminar (with possible separation zones) and may just start to exhibit transitional features without an extended turbulent region. To test this assumption, 3D ILES study of reference (14) employed a wing section with spanwise extension of 0.2c, with periodic conditions applied at the span tip planes. The comparative analysis employed a matrix of 2D and 3D case studies using the grid configurations shown in Table 1.

All computations discussed in the current work employ a physical time step of 0.3625×10^{-6} sec corresponding to the code non-dimensionalized time step of 9×10^{-5}. In the simulations, the steady-state flow conditions are first reached after marching for 200,000 steps. The pressure signals are then recorded for over 720,000 steps, hence collecting the data sample for 0.26 sec with the sampling rate of 62.7 kHz achieving the frequency resolution of Δf=3.83Hz.

4.1 Uniform Upstream Flow

The comparison of 2D and 3D ILES predictions was conducted in reference (14) for a test case selected from the measurements (2) performed for NACA0012 airfoil with the chord c=0.1m installed at the geometric angle of attack $\alpha=5^0$. In the numerical analysis, the calculations were performed for $\alpha=2^0$ to account for wind-tunnel corrections according to reference (15). The selected benchmark case corresponds to the mean flow velocity of 25 m/sec (M=0.072) with clean upstream flow. The analysis was conducted for Re_c=180,000 closely representing the experimental conditions.

The preliminary 2D study of reference (2) employed the baseline grid configuration, with the obtained results successfully validated against DNS analysis by Desquesnes et al (8). Furthermore, an excellent match of the predicted spectral peak frequencies against the feedback-loop formula was achieved.

2D and 3D ILES studies of reference (14) extended the 2D analysis of reference (2), with focus on investigating effects of various numerical parameters on the boundary-layer statistics and gaining further insight in the flow-acoustic interaction process. Results of the spectral analyses were examined in comparison with the experimental data (2) at the monitor points indicated by letters A, B, C (suction side) and C' (pressure side) in Fig. 3. Deviations were observed between the baseline and the fine grid configurations particularly on the upper surface towards the trailing edge but the comparison of the results obtained using the fine and the finest meshes (as specified in Table 1) showed minor differences. Hence, the fine mesh was employed in the subsequent numerical studies. Fig. 7 compares the spectra of the surface pressure time histories at the selected monitor points obtained using the fine meshes in 2D and 3D analyses. 3D results show a drop in the broadband levels accompanied by an overall better agreement with experimental data. This is particularly notable for some of the prominent tones although the overall comparison of tonal response predictions in 2D and 3D analyses may be considered satisfactory. Hence, this to a certain extent may justify the 2D assumption. At the same time, the results still exhibit significant differences with experiment in the broadband levels which may be related to the experimental installation effects, as indicated in reference (16).

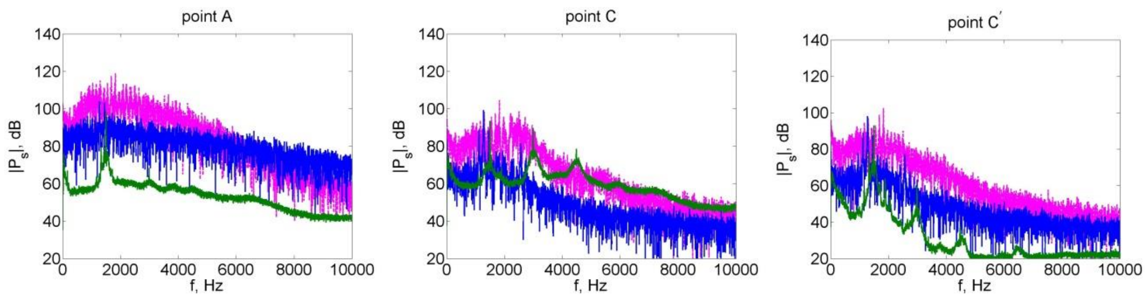

Figure 7 - Comparison of 2D (magenta) and 3D (blue) predicted (using fine meshes) vs. measured (green) airfoil surface pressure spectra at selected monitor points on suction and pressure sides.

For the baseline grid configuration, the mean pressure distributions have been previously validated against experimental data in reference (2). In Fig. 8(a), the RMS pressure distributions obtained from 2D simulations with baseline and fine meshes correspond well with one another and sustain the levels nearly to the trailing edge. In contrast, 3D results indicate a rapid decrease of RMS pressure amplitudes after reaching the peak levels, which appears to be related to the spanwise energy redistribution as illustrated further below. The peak RMS levels obtained using the fine mesh are similar in 2D and 3D computations but the grid differences are more pronounced in 3D results.

(a) (b) (c)

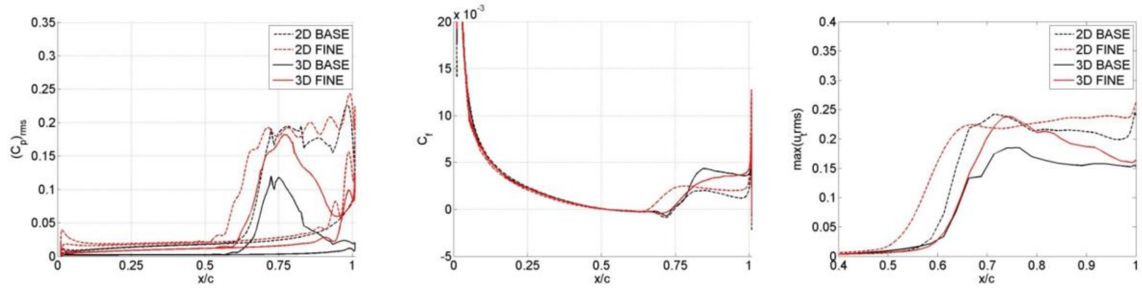

Figure 8 – (a) Airfoil surface RMS pressure distributions; Suction-side: (b) Skin friction coefficient, (c) Max(V_{t_RMS}).

Locations of the separated regions can be deduced from the surface distribution of the skin friction coefficient shown in Fig. 8(b) for the suction side. The separated regions appear to form at x=0.45c with a very thin separated layer, followed by a reattachment point at x=0.67. Fig. 8(c) quantifies the growth of the boundary-layer velocity fluctuations (indicative of instability growth) on the suction side by showing the predicted evolution of the RMS maxima for the tangential velocity components V_t. The maximum instability growth and saturation are clearly associated with the laminar separation zones. Note that the results correlate well with RMS pressure distributions shown in Fig. 8(a) exhibiting a pronounced decrease both in the pressure and velocity fluctuation levels in 3D analysis, in contrast to 2D results. Along the pressure side, the results (not shown) indicate much less noticeable boundary-layer dynamics except very close to the trailing edge where the formed separated region is accompanied by rapid growth of max(V_{t_RMS}) and RMS pressure (in Fig. 8(a)). Overall, the results indicate that both suction and pressure sides may contribute to the flow-acoustic resonant interactions in this flow regime.

(a) (b)

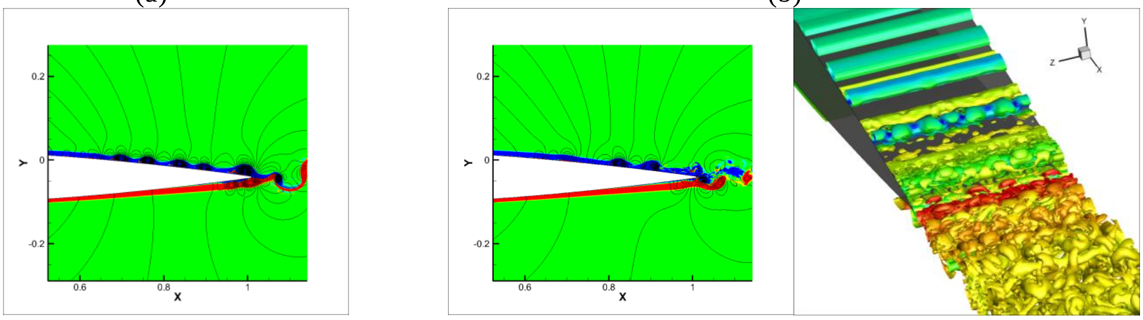

Figure 9 - Sample-averaged vorticity and pressure contours in (a) 2D study; (b) 3D study (including Q-criterion on the right)

The boundary-layer dynamics is further illustrated in Fig. 9 showing the sample-averaged vorticity (plus Q-criterion) and pressure contours obtained from 2D and 3D fine-mesh simulations. The appearance of the fine-scale vortical structures with strong spanwise redistribution towards the trailing edge in 3D studies (Fig. 9(b)) contributes to the corresponding reduction of RMS pressure and velocity levels observed in Figs. 8(a) and 8(c). The boundary-layer dynamics is also noticeable on the pressure side but very close to the trailing edge.

Reference (17) initiated numerical studies investigating effect of the upstream flow velocity in the range of 25 to 45 m/s on the feedback-loop process and the corresponding spectral response. Fig. 10 compares the latter results obtained in 2D study for the upstream velocity of 25 m/s against those obtained for 45 m/s, with the corresponding shift in the Re_c number between 180,000 and 325,000 (in contrast to reference (17) where it was kept constant). The primary tones in the surface pressure spectra are also shifted, and the tonal peak levels increase for 45 m/s in accordance to the pattern proposed by Lowson et al (18). The observed tonal shifts primarily scale with 0.8-power velocity dependence (typical of instability-produced acoustic signature). The shedding-dominated 1.5-power dependence associated with sudden jumps in the ladder-type frequency structure of primary tones (Fig. 1) does not easily reveal itself (in fact, not at all in Nash et al (19)), and this aspect will be re-visited in the next section.

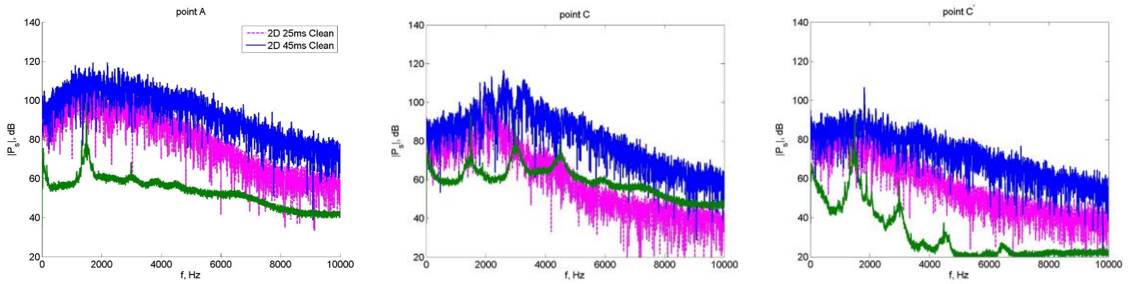

Figure 10 - Comparison of 25m/s (magenta) and 45m/s (blue) 2D-predicted airfoil surface pressure spectra at selected monitor points (measured results for 25 m/s are shown in green for reference).

4.2 Turbulent Upstream Flow

A novel method to introduce a turbulent flowfield in numerical simulations using a momentum source located in a region upstream of the airfoil (20, 21) and based on the random flow generation technique (22) was employed in reference (23) to study the effect of upstream flow non-uniformities on the flow-acoustic resonant interactions in NACA0012 airfoil. In the numerical experiments, the upstream turbulence, prescribed with non-dimensional integral length scale L=0.035 and intensities I=0.008 and 0.07, was continuously generated in order to collect sufficient statistical data for the spectral analyses.

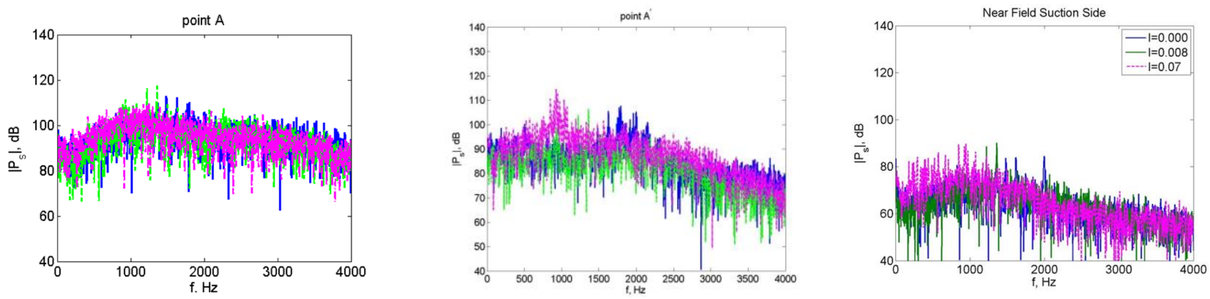

Figure 11 - Comparison of pressure spectra at selected monitor points for uniform and turbulent inflows.

Results in Fig. 11 compare the pressure spectra for the turbulent and uniform flow cases obtained at points A and A' symmetrically located near the trailing edge on the suction and pressure sides, correspondingly, and in the near field 2 chords above the trailing edge. Shifts in the dominant frequencies are notable, and it is also evident that the resonant interactions are not eliminated as a result of the impinging low-intensity turbulence with I=0.008. On the contrary, more prominent tones are observed for this case on the suction side compared to the case with the uniform upstream flow, with the frequency shift in the primary tones. For the higher turbulence intensity (I=0.07), the results indicate a complete suppression of prominent tones (and thus the acoustic feedback loop) in the suction-surface spectra due to the turbulent transition. Nonetheless, the tonal peaks are still present at point *A'*, which indicates that the feedback loop remains sustained on the pressure side contributing to the same frequency tones observed in the near field in Fig. 11. Both in the low-turbulence and uniform-flow cases, the spectral tonal contents appear rather close in points *A* and *A'* and the near field indicating that both sides develop similar acoustic feedback-loop characteristics.

Additional information may be derived from the instantaneous vorticity contours shown in Fig. 12. In the low-turbulence and uniform flow cases, the instability dynamics on the upper airfoil surface is phase-locked with acoustic modes in the feedback-loop mechanism that cuts on the distinct tones observed in Fig. 11. In contrast, in the high-turbulence case, the boundary-layer vorticity dynamics on the suction side observed in Fig. 12 is induced by the impinging uncorrelated turbulence modes through the phase-locking mechanism, and thus may only produce a broadband spectrum at point *A*.

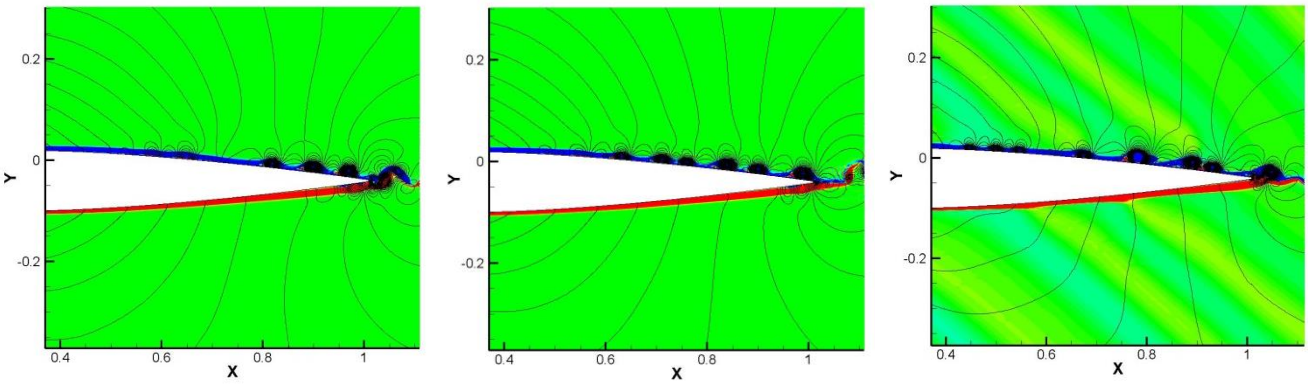

Figure 12 - Instantaneous vorticity contours for (left to right) uniform, low-turbulence and high-turbulence flow regimes.

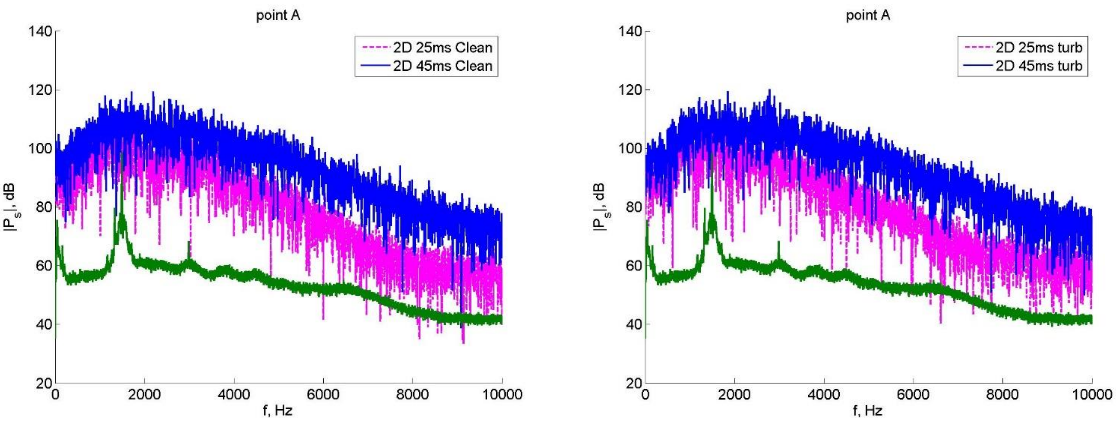

Figure 13 - Comparison of pressure spectra at point *A* for 25m/s and 45m/s predicted for uniform and low-turbulence (*I*=0.001) cases (measured results for 25 m/s are shown in green for reference).

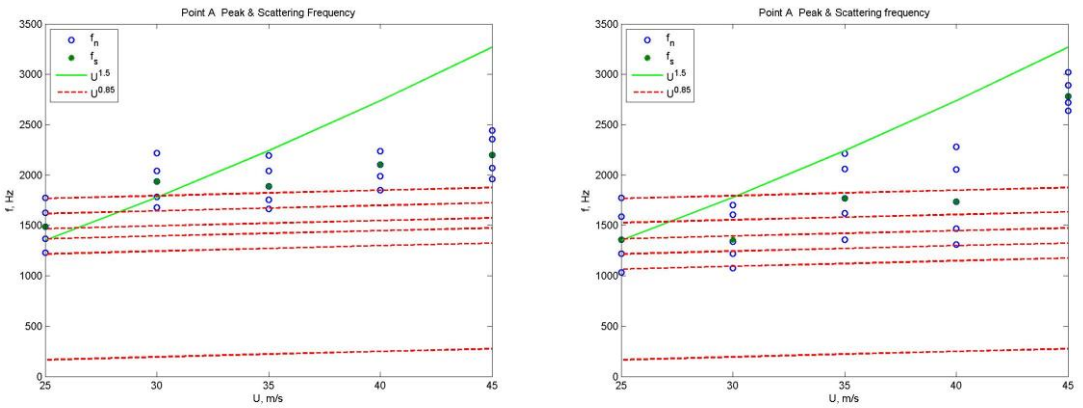

Figure 14 – Velocity dependence of peak frequencies at point *A* for uniform (left) and low-turbulence (*I*=0.001) (right) cases (primary tones are shown in closed circles).

To re-address the ladder-type velocity-dependence structure of the dominant tones (Fig. 1) and their sensitivity to the upstream flow conditions, Fig. 13 indicates that just a slight increase in the upstream turbulence level (with intensity *I*=0.001) may produce a notable rearrangement in the content of the tonal frequencies. The latter appears significant enough to reveal a jump in the velocity dependence of the primary tone to align with 1.5-power law at 45 m/s. Note that the shedding-frequency hump is observed even in the uniform-flow case but becomes more pronounced with a distinct tonal signature once a small turbulent excitation is introduced. Interestingly, this observation corresponds to that of

Nash et al (19) who attributed the persistently observed 0.8-power velocity dependence of the primary tonal frequency to their particularly clean experimental conditions. Different number of ladders in the tonal structures observed in different experiments may also be related to such sensitivity to the test environment.

To compare the growth of the boundary-layer velocity fluctuations in absence and presence of the upstream flow non-uniformities, Fig. 15 shows the predicted evolutions of the maxima of the RMS of the tangential velocity components V_t evaluated across the boundary layers on both airfoil sides.

(a) (b)

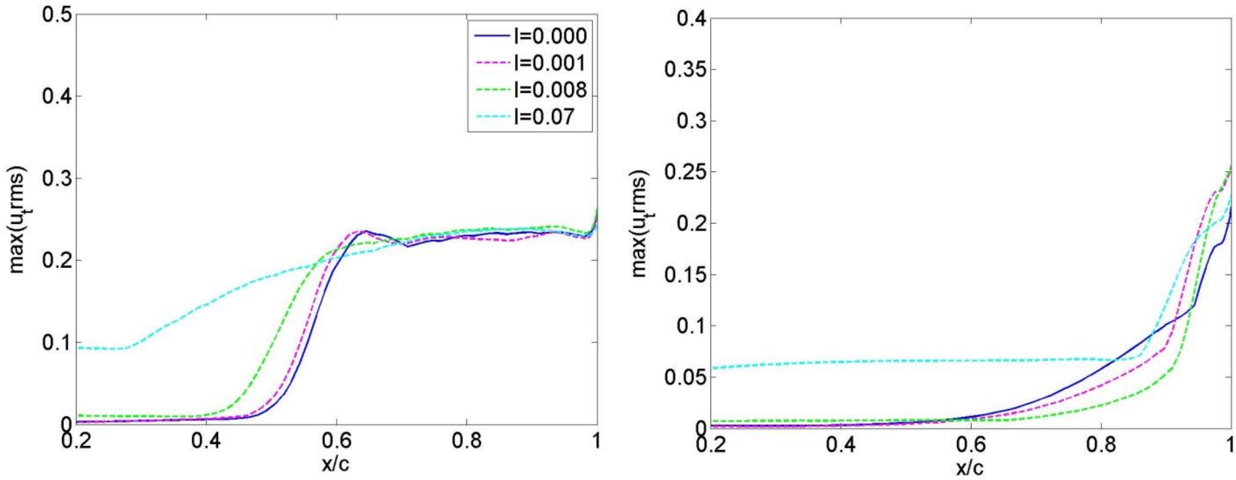

Figure 15 - Evolution of Max(V_{t_RMS}) along suction (a) and pressure (b) sides for turbulent vs. uniform upstream flow conditions.

As indicated above, the rapid growth of the RMS velocity amplitudes is closely correlated with the formation of thin laminar separation zones on both sides of the airfoil. The saturation of such growth appears to be linked to the flow reattachment. For the high-intensity turbulence case with I=0.07, much higher RMS levels are associated with fully turbulent flow conditions on the suction side where the laminar instabilities and the feedback-loop process are suppressed. In all the considered cases, the pressure side appears to sustain the flow-acoustic resonant interactions associated with the rapid instability growth through the separation regions forming close to the trailing edge.

Such findings are further substantiated by employing a linear stability analysis implemented in LASTRAC code (24) solving the linearized Navier-Stokes equations with the assumption of a quasi-parallel flow. The results based on the computed time-averaged boundary-layer tangential velocity profiles (supplied by the high-fidelity simulations) include the nondimensional growth rate of an instability mode and N-factor describing the normalized accumulated growth rate of the modal amplitudes integrated over a specified streamwise distance along the boundary layer. One may establish an analytical connection between the RMS and N-factor curves which is easily traced through comparison of Figs. 15(a) and 15(b) with, respectively, Figs. 16 and 17 describing the obtained N-factor curves for the cases of uniform and low-turbulence inflows. The latter show results of the linear stability analysis for, correspondingly, the suction and pressure side N-factors calculated for the instability modes with the highest spectral amplitudes at the trailing-edge locations and in the near field. For the suction side, the results indicate that the highest modal amplification rates are reached soon after the separation point and drop to near zero values close to the reattachment point, hence forcing the modal N-factors in Fig. 16 (and correspondingly the RMS curve in Fig. 15(a)) to plateau. Interestingly, the stability analysis describes a continuous growth of the N-factors from the point of instability inception, in contrast to the seemingly explosive growth of the RMS values in the separation region (Fig. 15(a)). At the same time, such analysis succeeds in predicting the dominant contributions of the primary frequency modes observed in the near-field tonal spectra in Figs. 7 and 11 both for the uniform and low-turbulence inflows. Note that the continued slight growth of the N-factors in Fig. 16 is due to the quasi-parallel flow assumption. A separate analysis conducted using LASTRAC code's more computationally-intensive non-parallel flow option generally compares well with the current results but reveals a saturation with a slight reduction of the N-factor levels in the post-reattachment region, thus more closely reproducing the RMS curve behavior in Fig. 15(a).

(a) (b)

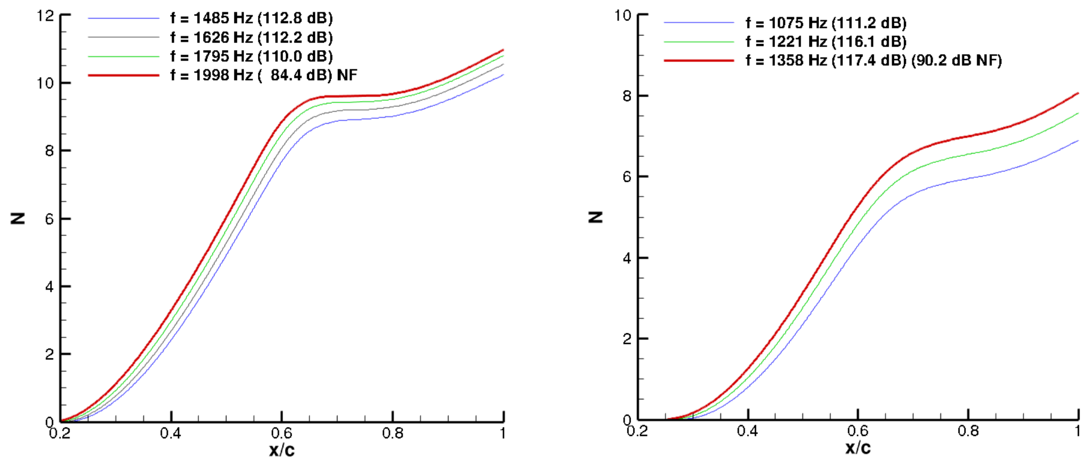

Figure 16 - Suction-side *N*-factors for selected frequency modes with the highest spectral amplitudes at point *A* and the near field, for uniform (a) and low-turbulence (I=0.008) (b) upstream inflows.

(a) (b)

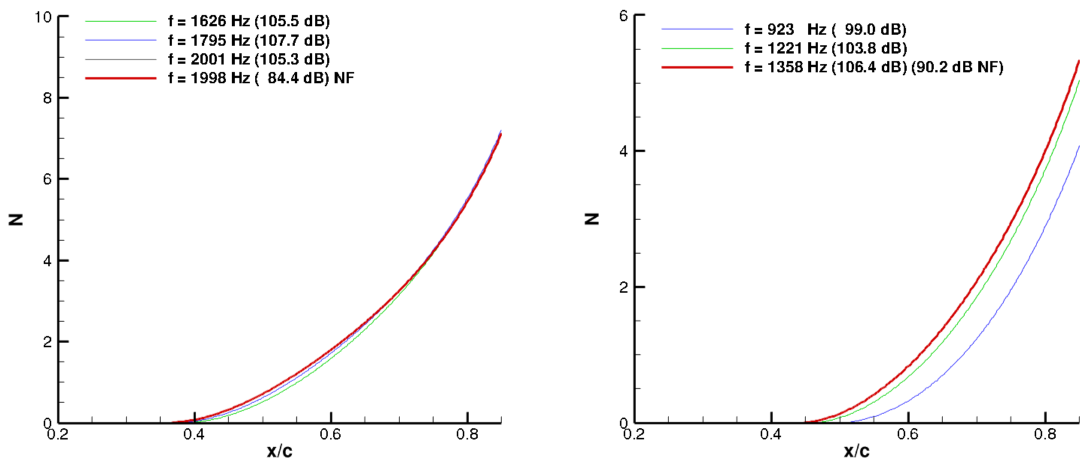

Figure 17 - Pressure-side *N*-factors for selected frequency modes with the highest spectral amplitudes at point *A’* and the near field, for uniform (a) and low-turbulence (I=0.008) (b) upstream inflows.

Figs. 17 illustrates the corresponding results of the linear stability analysis obtained for the airfoil pressure side. Note that the predictions of the *N*-factors compare well with the RMS curves in Fig. 15(b), and are similar for both uniform and low-turbulence cases indicating a rapid growth of the amplification rates and thus the instability amplitudes in the separated regions close to the trailing edge.

The frequency distribution of the *N*-factors accumulated at the points close to the trailing edge on the suction and pressure sides are shown in Fig. 18. The peak frequency of the airfoil near-field tonal response (in Fig. 11) is well-predicted by the stability analysis for the case of the uniform flow. However, the discrepancy appears to be larger for the low-turbulence case.

Finally, note that the accumulated modal growth rates appear lower in the turbulent inflow case on both airfoil sides in Figs 16 and 17, and thus the resulting tonal scattered acoustic levels are expected to be lower as well, in accordance to the preliminary results of the far-field acoustic studies.

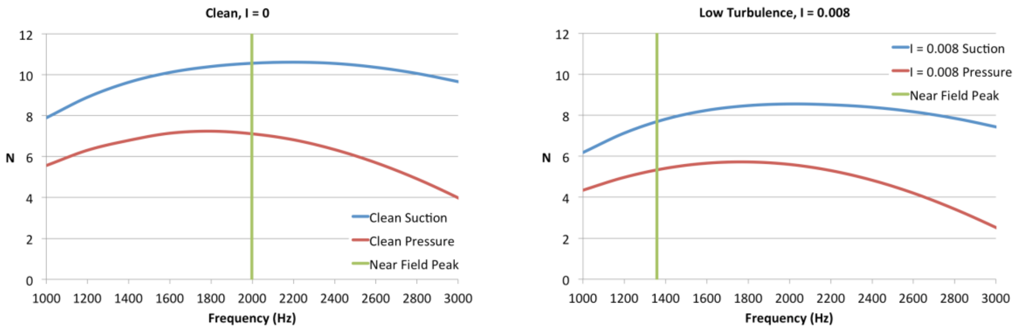

Figure 18 - *N*-factor frequency distribution on suction and pressure sides near the trailing edge, for (left to right) uniform and low-turbulence flow regimes (vertical lines mark the peak frequencies in the near-field spectra in Fig. 11).

5. CONCLUSIONS

Experimental and numerical studies of flow-acoustic resonant interactions in transitional NACA0012 airfoil installed at $\alpha=5^0$ were presented. With uniform upstream flow conditions, the experiments revealed a ladder-type structure of acoustic tones with dual velocity dependence corresponding to the rungs with frequency $f\sim U^{0.8\ldots0.85}$ related to the amplified instability-wave trailing-edge scattering, and the effectively produced vortex shedding corresponding to the dominant frequencies of each rung scaled with $f_s\sim U^{1.5}$. Introduction of a *weak* grid-generated upstream turbulence suppresses all tones associated with the acoustic feedback (0.8-power velocity dependence in the ladder-type tonal structure) while preserving the 1.5-power velocity dependence of the primary spectral hump.

High-accuracy numerical study compared the unsteady response predictions in the tones-generating transitional flow regime based on 2D and 3D ILES analyses. Effects of various numerical and physical parameters were investigated. In 3D ILES simulations, a significant drop in the broadband levels of the surface pressure response was observed along with an overall better agreement with experimental data, particularly notable for the prominent tones. The remaining discrepancy with experiment may indicate the necessity to more closely represent the experimental set-up in the numerical studies. Boundary-layer statistical moments showed an overall similarity between 2D and 3D analyses but 3D results indicated a rapid decrease of RMS pressure amplitudes after reaching the peak levels (with similar trend for the velocity fluctuations), which appeared to be related to the spanwise energy redistribution and appearance of fine-scale vortical structure observed in 3D analysis towards the trailing edge.

Studies of the effect of turbulent inflow with different intensity levels revealed notable shifts in the dominant frequencies of the unsteady airfoil response in the low-turbulence case and the suction-side suppression of the tones-producing acoustic feedback loop in the high-turbulence case. Analysis of the boundary-layer statistical moments indicated that both for the uniform and low-turbulence upstream flow conditions, the maxima of the velocity RMS amplitudes on the suction side were reached in the laminar separation zones. The growth saturation was linked to the flow reattachment occurring without subsequent turbulence transition thus enabling preservation of the coherent instability modes and the acoustic feedback mechanism. The results were substantiated by the linear stability analysis performed based on the sample-averaged boundary layer velocities on both sides of the airfoil. Such analysis confirmed the growth and saturation of the instability modes through the separated regions on either airfoil side, and was successful in matching the peak frequency of the airfoil near-field spectral response with the most amplified instability mode in the case of the uniform upstream flow. The accumulated modal growth rates appeared lower in the turbulent inflow case on both airfoil sides, which may result in the reduced scattered tonal acoustic levels.

ACKNOWLEDGEMENTS

Support for this work through Air Force Office of Scientific Research (Award Number FA9550-12-1-0126, Program Manager Dr. D. Smith), and Florida Center for Advanced Aero Propulsion is acknowledged.

REFERENCES

1. Raman G. Supersonic Jet Screech: Half-Century from Powell to the Present. Journal of Sound and Vibration 1999; 225: 543-571.
2. Colonius T. An Overview of Simulation, Modeling, and Active Control of Flow/Acoustic Resonance in Open Cavities. AIAA Paper 2001-0076.
3. Golubev VV, Nguyen L, Mankbadi RR, Roger M, Visbal MR. On Flow-Acoustic Resonant Interactions in Transitional Airfoils. Int. J Aeroacoustics 2014; 13(1): 1-38.
4. Paterson R, Vogt P, Fink M, Munch, C, Vortex Noise of Isolated Airfoils. J. Aircraft. 1973; 10:296-302.
5. Tam CKW, Descrete Tones of Isolated Airfoils, J Acoust Soc Am. 1974; 55: 1173-1177.
6. Arbey H, Bataille J, Noise Generated by Airfoil Profiles Placed in a Uniform Laminar Flow. J. Fluid Mechanics 1983, 134: 33-47.
7. Longhouse RE, Vortex Shedding Noise of Low Tip Speed Axial Flow Fans. J Sound and Vibration 1977; 53: 25-46.
8. Desquesnes M, Terracol M, Sagaut P, Numerical Investigation of the Tone Noise Mechanism over Laminar Airfoils, J. Fluid Mechanics. 2007; 591: 155-182.
9. Visbal MR., Gaitonde DV, On the Use of High-Order Finite-Difference Schemes on Curvilinear and Deforming Meshes. J. Computational Physics 2002; 181: 155–185.
10. Anderson DA, Tannehill JC, Pletcher RH, Computational Fluid Mechanics and Heat Transfer. McGraw-Hill Book Company 1984.
11. Visbal MR., Morgan PE, Rizzetta DP, An Implicit LES Approach Based on High-Order Compact Differencing and Filtering Schemes. AIAA Paper 2003-4098.
12. Lele SK, Compact Finite Difference Schemes with Spectral-like Resolution. J. Computational Physics 1992; 103: 16–42.
13. Wagner C, Huttl T, Sagaut P, Large-Eddy Simulation for Acoustics. Cambridge University Press 2007.
14. Golubev VV, Nguyen L, Mankbadi RR, Roger M, Visbal MR, Acoustic Feedback-Loop Interactions in Transitional Airfoils. AIAA Paper 2013-2111.
15. Brooks TF, Pope DS, Marcolini MA, Airfoil Self-Noise and Prediction. NASA RP-1218. 1989; 1-137.
16. Moreau S, Henner M, Iaccarino G, Wang M, Roger M, Analysis of Flow Conditions in Freejet Experiments for Studying Airfoil Self-Noise. AIAA Journal. 2003; 41: 1895-1905.
17. Golubev VV, Nguyen L, Mankbadi RR, Roger M, Dudley J, Visbal MR., On Self-Sustained Flow-Acoustic Resonant Interactions in Airfoil Transitional Boundary Layers. AIAA Paper 2013-2619.
18. Lowson MV, Fiddes SP, Nash EC, Laminar boundary layer aeroacoustic instabilities. AIAA Paper 94-0358.
19. Nash EC, Lowson MV, McAlpine A., Boundary Layer Instability Noise of Airfoils, J. Fluid Mechanics 1999; 382:27-61.
20. Golubev VV, Brodnick J, Nguyen L, Visbal MR, New Approach to Modeling Airfoil Interaction with Upstream Turbulence. AIAA Paper 2011-3899.
21. Golubev VV, Brodnick J, Nguyen L, Visbal MR, High-Fidlity Simulations of Airfoil Interaction with Upstream Turbulence. AIAA Paper 2012-3071.
22. Smirnov R., Shi S, Celik I, Random Flow Generation Technique for Large Eddy Simulations and Particle-Dynamics Modeling. Journal of Fluids Engineering 2001; 123: 359-371.
23. Golubev VV, Nguyen L, Mankbadi RR, Roger M, Pasiliao C, Visbal MR., Effect of Upstream Turbulence on Flow-Acoustic Resonant Interactions in Transitional Airfoils. AIAA Paper 2014-3303.
24. Chang C, Langley Stability and Transition Analysis Code (LASTRAC) Version 1.2 User Manual. NASA/TM-2004-213233, 2004.